Analyst

PAPER

Cite this: *Analyst*, 2020, **145**, 5861

Received 16th May 2020,
Accepted 8th July 2020

DOI: 10.1039/d0an00984a

rsc.li/analyst

Remote ablation chamber for high efficiency particle transfer in laser ablation electrospray ionization mass spectrometry†

Marjan Dolatmoradi, ‡[a] Jarod A. Fincher, ‡[a] Andrew R. Korte, [a]
Nicholas J. Morris [b] and Akos Vertes *[a]

Laser ablation electrospray ionization (LAESI) driven by mid-infrared laser pulses allows the direct analysis of biological tissues with minimal sample preparation. Dedicated remote ablation chambers have been developed to eliminate the need for close proximity between the sample and the mass spectrometer inlet. This also allows for the analysis of large or irregularly shaped objects, and incorporation of additional optics for microscopic imaging. Here we report on the characterization of a newly designed conical inner volume ablation chamber working in transmission geometry, where a reduced zone of stagnation was achieved by tapering the sample platform and the chamber outlet. As a result, the transmission efficiency of both large (>7.5 μm) and smaller particulates (<6.5 μm) has increased significantly. Improved analytical figures of merit, including 300 fmol limit of detection, and three orders of magnitude in dynamic range, were established. Particle residence time, measured by the FWHM of the analyte signal, was reduced from 2.0 s to 0.5 s enabling higher ablation rates and shorter analysis time. A total of six glucosinolates (sinigrin, gluconapin, progoitrin, glucoiberin, glucoraphanin, and glucohirsutin) were detected in plant samples with ion abundances higher by a factor of 2 to 8 for the redesigned ablation chamber.

Introduction

Ambient ionization mass spectrometry (MS) has become a powerful tool due to its capability in "the analysis of unprocessed or minimally modified biological samples *in situ*" without perturbations to the system's natural environment.[1,2] Currently available ambient ionization techniques, such as desorption electrospray ionization (DESI), direct analysis in real time (DART), laser ablation electrospray ionization (LAESI), and rapid evaporation ionization mass spectrometry (REIMS) provide innovative ionization methods for direct analysis of biological tissues in ambient environment under native conditions.[3–6]

However, in ambient ionization mass spectrometry, close spatial proximity between the sample and the mass spectrometer inlet is often required, restricting the location, size and geometry of the sample to be analyzed.[7,8] Several ambient ionization techniques have been developed to surpass the limitation due to sampling geometry using aerodynamic and hydrodynamic ejectors/injectors (pneumatic assistance) to promote the transport of neutrals and ions. For example, remotely operated REIMS coupled with an electrosurgical tool (the active electrode) utilizes the aerosol by-product of thermal tissue ablation for the online analysis of samples, providing real-time histological information at the point of dissection.[9–11] Another example is infrared matrix-assisted laser desorption electrospray ionization (IR-MALDESI) integrated with a remote analyte sampling, transport and ionization relay (RASTIR) device.[12,13]

Numerous laser ablation (LA) chambers have been developed for inductively coupled plasma mass spectrometry working with high energy UV laser pulses.[14,15] However, plumes generated by mid-IR lasers from biological samples have significantly different characteristics in the size distribution and velocity of the generated particles. For example, in mid-IR ablation of frozen glycerol targets, the particle size distribution (PSD) shifts to higher number densities with increasing fluence.[16] Therefore, designing and refining dedicated ablation chambers for mid-IR lasers and biological samples is needed.

In LAESI, the laser ablation of water-rich samples in the mid-IR region (2.94 μm) induces surface evaporation at near or

---

[a] *Department of Chemistry, The George Washington University, WashingtonDC 20052, USA. E-mail: vertes@gwu.edu; Fax: +1 (202) 994-5873; Tel: +1 (202) 994-2717*

[b] *UES, Inc., Beavercreek, OH 45432, USA*

† Electronic supplementary information (ESI) available. See DOI: 10.1039/d0an00984a

‡ These authors contributed equally to this work.

below the ablation threshold and a much more efficient material ejection through phase explosion at higher laser fluence levels, resulting in μm-sized particulates and spallation of fragments.[17,18] In a remote ablation chamber, a nonreactive carrier gas (*e.g.*, N_2) transfers the laser generated plume from the ablation site to the MS inlet where they are intercepted and ionized by an electrospray. The ablation chamber should (i) minimize the loss of particulate and permit their quantitative transport, and (ii) lead to a rapid transport from the ablation site to the MS inlet to minimize particle residence times in the chamber, particle–particle and particle–wall interactions, pulse mixing, and signal tailing induced during the transport.[19] The residence time of particulates not only depends on the shape and volume of the ablation chamber, but it is also governed by the carrier gas pressure, velocity, and flow pattern, as well as the size distribution and momentum of particles inside the chamber.[20]

Previous studies of remote LAESI ablation platforms have demonstrated that the perpendicular orientation of the gas flow and the ablation plume in the prolate spheroid ablation chamber reduced the transfer efficiency to 27% compared with conventional LAESI. The conical inner volume ablation chamber with coaxial orientation of the carrier gas flow and ablation plume not only recovered the losses observed in the first platform, but also improved the number of metabolite peaks detected from biological tissues. However, a large region of stagnation still existed in front of the sample platform resulting in trapping of the small particles.[2,21]

A significant challenge in remote sampling MS platforms is the sample loss caused by deposition of large particles on the inner walls of the chamber and transfer tube. Because of this, the initial PSD and velocity distribution, determined by the ablation process and the optical and mechanical properties of the sample, become important factors in the efficiency of transmission. Depending on the geometry of the chamber and the transfer tube, the high end of the PSD is cut off during transfer, *e.g.*, by sharp turns in the gas flow.[22] Conversely, the low end of the PSD can be prone to areas of stagnation by trapping the smallest particle in dead zones. The impacts of particle deposition resulting in reduced transfer efficiency and longer residence times can be mitigated by shaping the PSD of the aerosol produced by the laser ablation. The interior geometry of the ablation chamber and transfer tube in combination with the dynamics of plume expansion and carrier gas flow are also significant factors.[20,23,24] For example, production of laminar flow allows for efficient transport of ablation plume over long distance and keep the sample material away from redepositing onto the transfer tube and chamber inner walls.[2]

Here, we report an improved ablation chamber design working in transmission geometry with better gas dynamics compared to the previous conical inner volume chamber. Particle trajectory simulations were performed to identify potential losses in transfer efficiency. Computational fluid dynamics (CFD) modelling, was used to simulate gas flow and particle transfer within the studied ablation chambers. Regions of stagnation were linked to the cylindrical shape of the sample platform, and sedimentation due to high gas velocity was observed in the transition between the chamber and the transfer tube. These were identified as major sources contributing to loss in transfer efficiency. To overcome these shortcomings, rapid prototyping of a newly designed ablation chamber was performed, incorporating modifications derived from CFD modelling. A reduced zone of stagnation, achieved by tapering the sample platform, and better transition between the chamber and the transfer tube improved the analytical figures of merit, including lowering the limit of detection (LOD), widening the dynamic range, and shortening the residence time.

Experimental

Chemicals

HPLC-grade water (W6-212), methanol (A456-4), and chloroform (C607-4) were purchased from Alfa Aesar (Ward Hill, MA, USA). Glacial acetic acid (A35-500) was acquired from Fisher Scientific (Waltham, MA, USA). Verapamil hydrochloride (V4629) and gelatin from bovine skin (G9391) were obtained from Sigma-Aldrich (St Louis, MO, USA).

Sample preparation

To have uniform targets with known concentrations of an analyte and controlled thickness, tissue phantoms were prepared using 5% (w/v) gelatin dissolved in HPLC-grade water and mixed with predefined amounts of verapamil. These mixtures gelled at room temperature after ∼10 min. For the limit of detection (LOD) measurements, they were sectioned to 60 μm thick slices in a cryomicrotome (CM1800, Leica Microsystems Inc., Nussloch, Germany) at −18 °C.

Brussels sprouts (*Brassica oleracea*) were purchased from a local supermarket, cryosectioned to 60 μm thickness and thaw-mounted on a 0.5 mm-thick quartz coverslip moisturized with a few drops of water. Excess water was removed from the backside of the coverslip to eliminate the absorption of the laser beam by water residues.

Computational fluid dynamic modelling

The Navier–Stokes equations provided the mathematical model at the macroscopic level to describe the spatial and temporal variations of gas flow properties, such as velocity, density, temperature, and pressure distributions, in a given geometry, and to distinguish laminar and turbulent flows.[25] A CFD solver module of SolidWorks (Flow Simulation 2015, Dassault Systèmes, Vélizy-Villacoublay, France) was used to perform the gas dynamic simulations inside the modified and previously designed conical inner volume ablation chambers.

The finite volume method (FVM) was applied to solve the Navier–Stokes equations using a locally refined adaptive mesh. The carrier gas was considered as an ideal gas and modelled as a steady-state flow field in the simulations. Convergence criterion was also set as eight travels of gas volume elements through the chamber. Mach numbers, calculated at the boundaries (gas inlets and outlets), showed that the flow pattern throughout the chambers was subsonic. The outlet was held at constant environmental pressure for both chambers. Inlet boundary conditions were entered as mass flow rates calculated from the experimentally observed optimal volumetric flow rates.

Particle trajectory simulations

To evaluate the entrainment and transport of material from a mid-IR laser-induced ablation in our remote LAESI platforms, the trajectories of these particles in the previously reported conical inner volume ablation chamber were modeled using CFD-based particle trajectory simulations. The modelled chamber was coupled to a 60 cm long transfer tube (i.d. 3 mm) with a connector (i.d. 1 mm). This computational analysis was performed to identify major sources of sample loss through redeposition of material onto the inner walls of the chamber and tube. The investigated particle sizes were chosen based upon PSD measurements for mid-IR laser ablation in reflection geometry.[26] The initial velocities in our modeling were based on in-depth plume dynamics measurements of mid-IR laser ablation.[27]

The conical inner volume ablation chamber consisted of a platform to accommodate samples up to 7.5 mm in diameter. It was designed in SolidWorks 2015 (Dassault Systèmes, Vélizy-Villacoublay, France) and 3D printed from proprietary Stratasys material (VeroClear RGD810) using Stratasys Object260 Connex3 printer. The chamber structure was built *via* inkjet printing heads with layer-by-layer UV curing. The inlet and outlet ports were tapped for the desired fitting. The support material used during printing was removed *via* water jet.

Laser, electrospray, and mass spectrometer

Details of the homebuilt ion source used for conventional and remote LAESI-MS analysis have been described.[2,3,21] Briefly, a Nd:YAG laser driven optical parametric oscillator (Vibrant IR, Opotek, Carlsbad, CA) with 4 ns pulse length, 2.94 μm wavelength, and 10 Hz repetition rate was coupled to the sample mounted on a quartz coverslip. The laser beam was focused through a 100 mm focal length CaF_2 plano-convex lens (LA5817, Thorlabs, NJ, USA), producing a spot size of ~300 μm. This spot size was selected to test the chamber, and it did not represent a limitation for spatial resolution. The movement of the sample stage was controlled by an XY translation stage in the focal plane of the laser.

The electrospray solution consisted of 50% methanol acidified with 0.1% glacial acetic acid (v/v) in positive ion mode, and 2 : 1 methanol/chloroform solution in negative ion mode. It was supplied by a syringe pump (Physio 22, Harvard Apparatus, Holliston, MA, USA) at 400 nL min^{-1} through a stainless steel emitter (MT320-100-5-5, i.d. 100 μm, New Objective, Woburn, MA, USA). The emitter was positioned on axis with the inlet orifice at a distance of 10 mm. High DC voltage of −2600 V in negative ion mode and +3500 V in positive ion mode was generated by a high voltage power supply (PS350, Stanford Research Systems, Sunnyvale, CA, USA).

All LAESI-MS measurements were acquired using a Q-TOF Premier mass spectrometer (Waters Co., Milford, MA, USA) in single reflectron mode and processed using MassLynx (version 4.1, Waters Co., Milford, MA, USA), and Origin 2018 (OriginLab Corporation, Northampton, MA, USA) software packages. For the identification of Brussels sprout metabolites, collision induced dissociation (CID) MS/MS spectra were acquired at 20–25 eV collision energy.

The aerosol of ablated material was transported from the ablation chamber to the electrospray near to the mass spectrometer inlet using a flexible polymer tube (i.d. 3 mm, length 60 cm) at a right angle. Phthalate-free Tygon stock (E-3603, U. S. Plastic Co., Lima, OH, USA) was used for transfer tube to minimize contamination and MS background. The tube outlet-emitter geometry is defined by the gap between the transfer tube outlet and the electrospray axis (15 mm), and by the gap between the tube axis and the emitter tip (2 mm). The selected distance between the transfer tube and the electrospray axis represents a tradeoff. At too large distances, particle capture by the electrospray is inefficient, whereas at too short distances the gas flow disrupts the electrospray.

All geometric parameters for the previous ablation chamber were optimized before analysis. Illustration of the newly designed conical inner volume ablation chamber and the overall experimental setup is shown in Fig. 1.

Results and discussion

Gas dynamics calculations in conical inner volume chambers

Velocity vector plots illustrating gas flow dynamics throughout the previously reported conical ablation chamber assembled with tapered and non-tapered transfer tube connectors can be found in Fig. 2. The axial midplane views show the gas flow at ~2 m s^{-1} entering through the two antipodal inlets and being decreased in velocity due to the expansion into a relatively large volume around the sample platform.

Comparing Fig. 2a and b highlights the mismatch in the inner diameter of the connector between the chamber and the transfer tube. In Fig. 2a, a sudden decrease in the diameter at the chamber connector interface results in an abrupt increase in the gas velocity and a change in flow direction, which are expected to be detrimental to the transfer of larger particles (similarly to the initial stages in a cascade impactor).[28] In contrast, in Fig. 2b the lack of diameter change at that same interface results in a smooth transition in the velocities benefiting the transfer of larger particles. The velocity profile inside the tapered connector stays smooth in its entire volume and transitions to the transfer tube without a sudden change.

Fig. 2c highlights the effects of the conical sample platform on the gas flow. In comparison to Fig. 2b, the most important difference can be observed in front of the sample platform. In the previous design, there is a stagnation area comparable in size with the platform itself. Moreover, in the center, the direction of the gas flow opposes the direction of the plume expansion induced by the laser ablation. In contrast, in Fig. 2c the

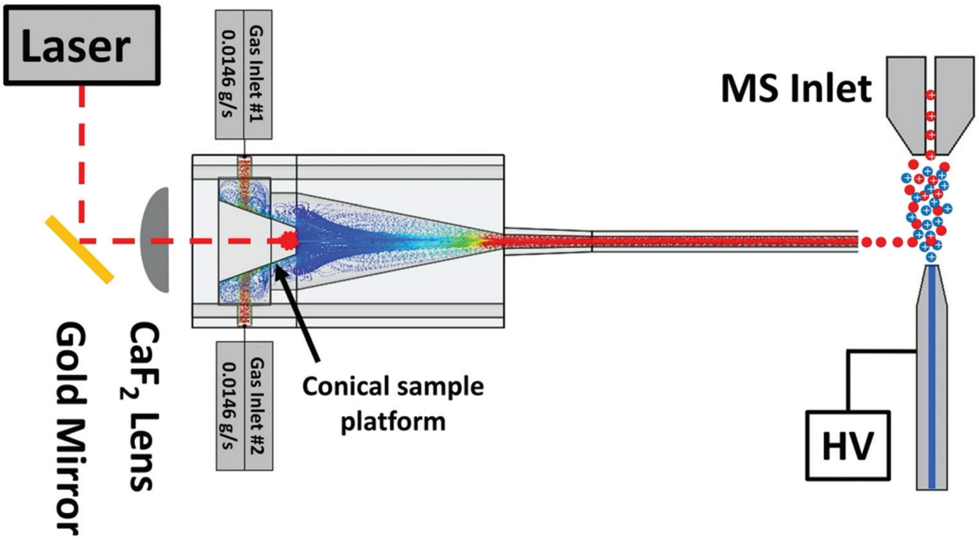

Fig. 1 Schematic of remote LAESI setup for newly designed ablation chamber with a conical sample platform. The carrier gas flow (dots) travels through the chamber coaxially with the freely expanding laser ablation plume produced in the center of the sample platform.

flow pattern around the conical sample platform exhibits a significantly reduced area of stagnation and a minimized counterflow in the center.

Flow patterns inside the modified ablation chamber (Fig. 2c) show that the strong turbulence present at the gas inlet was decreased by the sample platform, and robust laminar gas flow was obtained in the rest of the chamber.

Particle trajectories and transfer efficiencies

In order to analyze particle trajectories and transfer efficiency, an initial PSD, uniform in the 5 to 10 μm region, was defined. Particles starting from the center of the sample platform, where the laser was focused, with initial velocities of 100, 150, and 200 m s^{-1}, exhibiting isotropic directional distribution in front of the ablation site, were followed by the CFD model.

In Fig. 3, the particle trajectories for 5 and 9 μm particle sizes starting isotropically with uniform initial velocities of 150 m s^{-1} without and with the conical sample platform were compared *in silico* using CFD software. Tracking of 9 μm particles for the two platforms shows that in both cases the initial momentum carries them on straight trajectories and eventually some of them are entrained by the gas flow (see Fig. 3b and d). The most divergent fraction of these particles hit the chamber wall and remain there. This observation indicates that heavy-particle trajectories are independent of the platform geometry.

As shown in Fig. 3a, the 5 μm particles follow mixed fate in front of the cylindrical platform. Some particles are transported straight out of the chamber, whereas others are confined by the large zone of stagnation in front of the platform. However, in Fig. 3c, the significantly reduced zone of stagnation allows more of these particles to escape and leave the chamber.

As the initial velocities of the particles ejected by laser ablation (*e.g.*, 150 m s^{-1}) are much higher than the gas velocity inside the chamber (<6 m s^{-1}), a hypothetical particle stopping distance can be calculated by a simple drag model.[29] The calculations indicate that mid-IR laser-ablated 5 μm particulates, slowed by the drag force, travel up to 1.1 cm away from the ablated surface. At that stage, the gas flow takes over and carries the particle along the flow lines. However, in the original design this is still inside the dead zone (see Fig. 3c) resulting in trapping of these small particles in front of the sample platform.

Overall transfer efficiencies reflecting the portion of trajectories that arrived at the transfer tube were calculated. Percent particle transfer efficiencies as a function of particle size for the three different chambers are shown in Fig. 4. Modelling the chamber with a 1 mm i.d. connector (not tapered) and a transfer tube of 3 mm i.d. and L = 60 cm length, the corresponding curve in Fig. 4 (triangle symbols) indicated that the PSD was truncated both at the low and the high end and the overall transfer efficiency was 53%. Introducing a tapered connector (round symbols in Fig. 4) resulted in significantly higher transfer efficiencies for larger particulates (>7.0 μm) but somewhat lower transfer efficiencies for small particles (<7.0 μm) and the overall transfer efficiency improved to 68%. Major differences between these two designs are in the flow pattern at the interface between the chamber and the connector piece. Previous studies on remote ablation chambers for ICP-MS indicated that large-sized particles were mostly lost at higher gas flow rates.[14,30]

For the original ablation chamber with the tapered connector, examination of simulated particle fates revealed that the large stagnation region in front of the sample platform significantly reduced the capture efficiency of smaller particles (*e.g.*, at 5 μm), as they lacked the initial momentum to overcome the

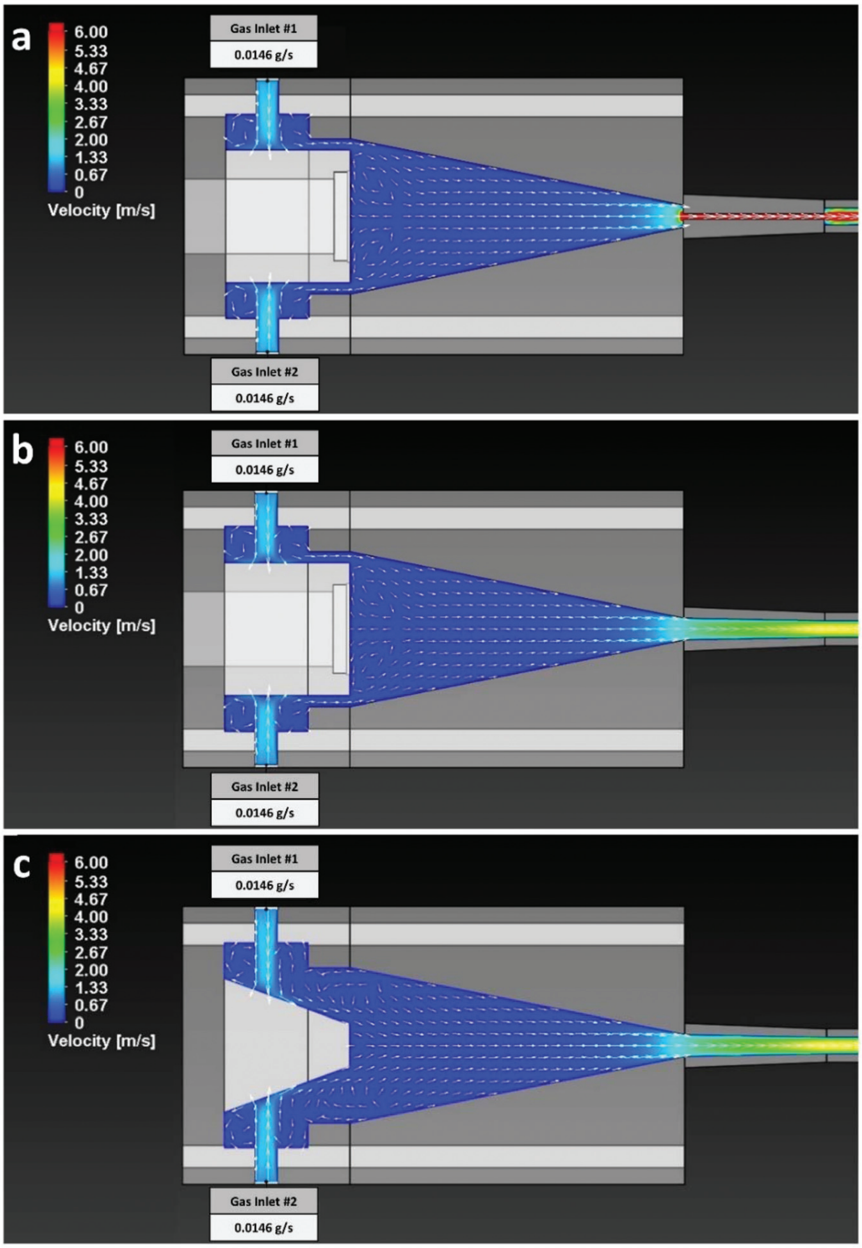

Fig. 2 Velocity vector plots in an axial midplane with vectors illustrating gas flow directions and false color scale indicating velocity amplitudes throughout (a) previously reported conical inner volume chamber (original) assembled with mismatching small diameter connector and a 60 cm long transfer tube, (b) ablation chamber assembled with a tapered connector to transfer tube, and (c) a redesigned ablation chamber with a conical sample platform.

low-velocity backflow and reach the higher-velocity laminar flow regions, where they could be entrained. This explains the drop in transfer efficiency for the smaller particles in Fig. 4. To mitigate this issue, the geometry of the sample platform was modified to a conical shape that minimized the dead zone directly ahead of the sample. Using a conical sample platform dramatically reduced the region of stagnation at the sample interface, leading to an overall 85% transfer efficiency (Fig. 4). This modification led to a significant enhancement in the entrainment of 5 μm particles (*i.e.*, with less momentum) resulting in an overall transfer efficiency increase from 52% to 100%.

Figures of merit

To characterize the redesigned ablation chamber for LAESI, we need to explore its ability to retain the original PSD produced by the ablation (see Fig. 4), potential improvements in dynamic range, and the reduction in the analyte residence time following a laser pulse.[20]

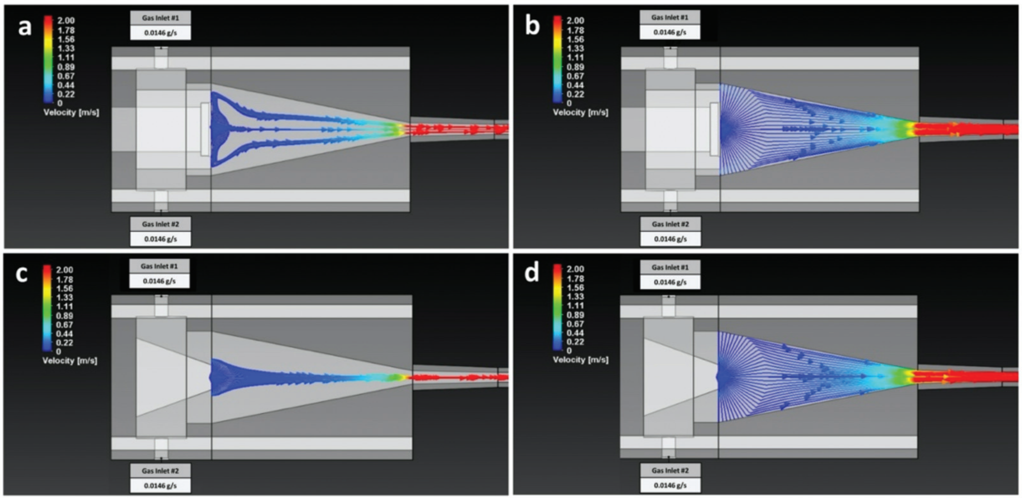

Fig. 3 Simulated trajectories for 5 and 9 μm particles starting with uniform isotropic initial velocities of 150 m s^{-1} in original ablation chamber (a) and (b), respectively, and in redesigned ablation chamber with conical sample platform (c) and (d), respectively.

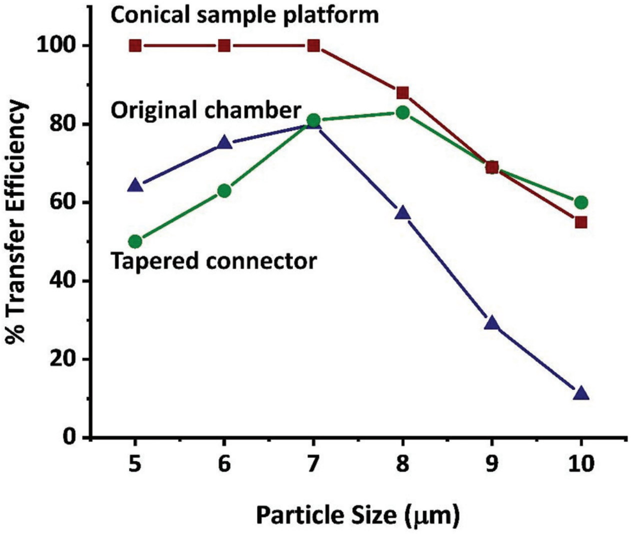

Fig. 4 Particle transfer efficiencies as a function of particle size for original ablation chamber with non-tapered (▲) and tapered (●) transfer tube connector and modified ablation chamber (■). The modified chamber does not affect the transfer efficiency for particle sizes greater than 9 μm. Average values of transfer efficiency were calculated for velocities 100, 150, and 200 ms^{-1} and plotted as a function of particle size. Only the points indicated by symbols are measured datapoints.

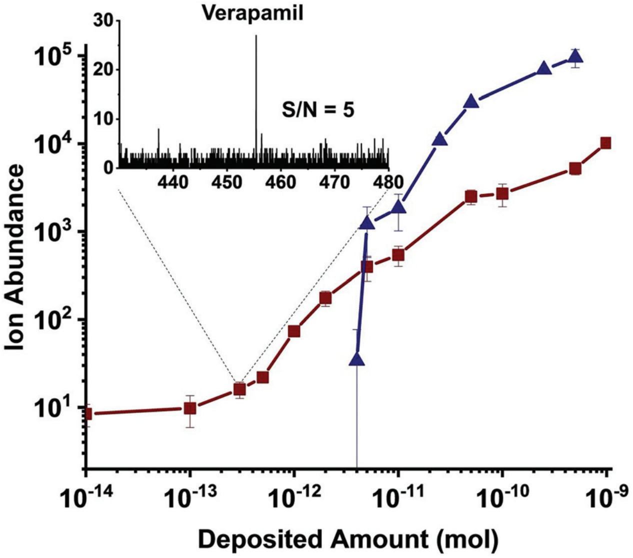

Fig. 5 Comparison of ion abundances by remote LAESI-MS from a tissue phantom made of verapamil-infused gelatin as a function of loading for original (▲) and modified (■) ablation chambers. Inset shows S/N ratio of 5 at the limit of detection for the modified ablation chamber. Only the points indicated by symbols are measured datapoints.

To determine the LOD in the new ablation chamber, a tissue phantom made of a 60 μm thick verapamil-infused gelatin section was analyzed at different verapamil concentrations. Signal was acquired from an area of 0.48 mm^2 by moving the tissue phantom to expose fresh areas to the ablating laser for analysis. The comparison between the original chamber and the current one with the conical sample platform shows a significant improvement in the limit of detection (LOD) from a minimum loading of 8 pmol to 300 fmol, respectively (see Fig. 5). Whereas at high loadings (at >5 pmol) the signal from the original chamber exceeds that of the redesigned chamber, at lower loadings the latter shows superior signal. As a result, the new chamber also exhibits a dynamic range increase to three orders of magnitude from the two orders of magnitude obtained for the original chamber.

Analyte residence time was determined by measuring the temporal profile of the verapamil ion signal following a single laser pulse. As shown in Fig. 6, the temporal profile shows 0.5 s at FWHM for the verapamil ion, whereas it is 2.0 s for the previous design, a factor of four decrease. The LOD improve-

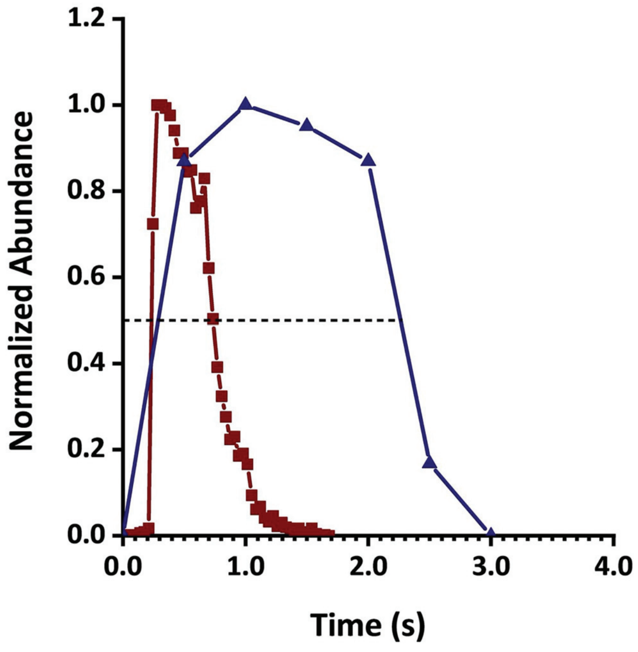

Fig. 6 Temporal profiles of verapamil signal after a single laser pulse impinging on tissue phantom for original (▲) and modified (■) ablation chambers indicate reduced residence time. Only the points indicated by symbols are measured datapoints.

ment, however, was not a result of this shorter temporal profile. It stemmed from the more efficient particle transport due to the reduced zone of stagnation in front of the sample platform and better passage between the chamber and the transfer tube. Indeed, the comparison of verapamil ion yields between the original and modified ablation chambers showed an improvement in sensitivity by a factor of ∼27 (see Fig. 5), whereas the residence time of the analytes is only four times shorter than in the original chamber. Repeated measurements of the temporal profiles also indicated an improvement in the reproducibility of the residence time characterized by its RSD reduced from 31% to 15% (Fig. S1†). The temporal profile of verapamil signal for four single laser pulses impinging on the tissue phantom indicated no sample carryover.

Remote LAESI of metabolites in plant tissue

To test the performance on a real-world sample, Brussels sprout stem sections were analyzed using both the original and the conical sample platform ablation chambers. The 60 μm thick sections were analyzed using a laser fluence of 7.1 J cm^{-2}. For an accurate comparison of the two platforms, 550 laser shots were fired per sample, corresponding to 10 shots per scan.

To demonstrate improved molecular coverage, the zoomed-in spectra, obtained from the ablation of Brussels sprout stem section using the original and redesigned ablation chambers, were compared (see Fig. S2†). After background subtraction by MassLynx, a total of 129 and 106 peaks were detected for the new and original chambers, respectively. After deisotoping using the mMass software, 64 and 55 sample related peaks were detected, corresponding to sugars, lipids, and glycosides, for the new and original chambers, respectively (see Fig. 7). For both platforms, a total of six glucosinolates (sinigrin, gluconapin, progoitrin, glucoiberin, glucoraphanin, and glucohirsutin) were detected with stronger ion abundances by a factor of two to eight (see Table 1) for the redesigned ablation chamber. The confirmation of peak assignments was based on accurate mass (see Table 1) and tandem mass spectra (Fig. S3†).

Analysis of glucosinolates is important because they are secondary metabolites that serve as defense compounds against herbivores, exhibit regulatory functions in inflammation, stress response, antioxidant activities, as well as antimicrobial properties.[31,32] The glucosinolates and the myrosinase enzyme serve as an activated plant defense system, in which myrosinase is released upon tissue damage, *e.g.*, insect attack, and it hydrolyses the glucosinolates to biologically active molecules known as mustard oils. Many of these products are highly

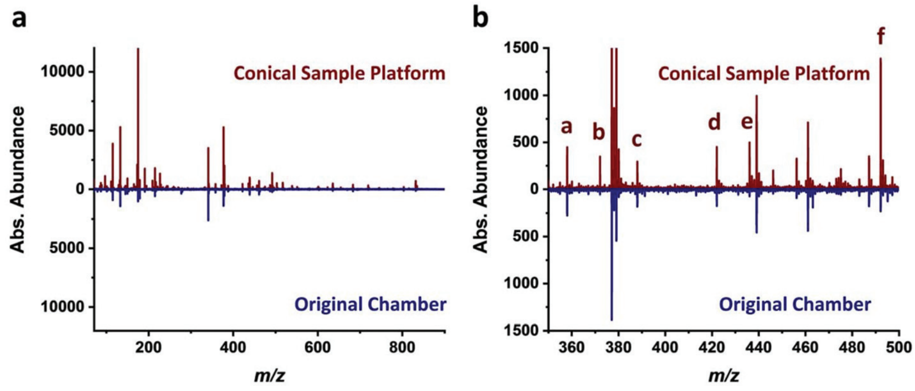

Fig. 7 (a) Mass spectra obtained by remote LAESI in negative ion mode from Brussels sprout (*B. oleracea*) stem sections using original and modified (conical sample platform) ablation chambers. After background subtraction and deisotoping, 64 and 55 sample related peaks were detected for the modified and original chambers, respectively, corresponding to sugars, lipids, and glycosides. (b) A total of six glucosinolates (sinigrin, gluconapin, progoitrin, glucoiberin, glucoraphanin, and glucohirsutin) were identified for both chambers.

Table 1 List of glucosinolates detected in Brussels sprout stem sections by remote LAESI-MS in negative ion mode. Glucosinolate identities were verified by tandem MS. Enhancement factors, $I_{\text{modified}}/I_{\text{original}}$, reflect improved ion abundances for the modified *vs.* original chamber design

Compound name	Chemical formula	Measured (m/z)	Calculated (m/z)	Δm (mDa)	$I_{\text{modified}}/I_{\text{original}}$
Sinigrin	$[C_{10}H_{17}NO_9S_2 - H]^-$	358.0292	358.0272	2.0	1.8
Gluconapin	$[C_{11}H_{19}NO_9S_2 - H]^-$	372.0507	372.0429	7.8	6.9
Progoitrin	$[C_{11}H_{19}NO_{10}S_2 - H]^-$	388.0379	388.0372	7.0	1.6
Glucoiberin	$[C_{11}H_{21}NO_{10}S_3 - H]^-$	422.0157	422.0249	−9.2	2.7
Glucoraphanin	$[C_{12}H_{23}NO_{10}S_3 - H]^-$	436.0294	436.0406	−11.2	7.9
Glucohirsutin	$[C_{16}H_{30}NO_{10}S_3 - H]^-$	492.1132	492.1032	10.0	6.4

toxic to a wide range of organisms including fungi and insects.[33] Knowing the levels and molecular forms of glucosinolates in plant tissue can inform about organismal fitness.

Conclusions

The revised ablation chamber with conical sample platform for remote LAESI-MS offers significant enhancements over earlier designs. It captures and entrains the mid-IR laser ablation plume more efficiently resulting in higher transfer efficiency and lower LOD. As a consequence, metabolite ion abundances are increased, and the residence times of the analytes are substantially reduced. The latter is important to reduce overall time requirements in future imaging applications.

Given that tissue ablation by mid-IR lasers is dependent upon the water content of the sample, its dehydration is a limiting factor. Thus, further improvements of this platform can include the incorporation of a Peltier stage for cooling to prevent dehydration.

Moving from local analysis to molecular imaging by MS requires integration of an automated XY translation stage with the modified ablation chamber. This will enable exploring compositional variation in live tissues at atmospheric pressure. As the signal per laser shot persists for ~2 s (see Fig. S1†), a 100 × 100 = 10 000-pixel imaging experiment can be conducted in 167 min. This is quite slow compared to current MALDI imaging rates. A remote ablation chamber better suited for MS imaging would require a different chamber design with shorter residence times.

In sum these results contribute to the development of atmospheric pressure remote ablation chambers for mid-IR lasers.

Conflicts of interest

There are no conflicts to declare.

Acknowledgements

The authors are thankful to Laith Samarah for helping with the initial setup of the experiments. This work is supported by the National Science Foundation Plant Genome Program under grant no. IoS-1734145 awarded to G. S.

References

1 C. L. Feider, A. Krieger, R. J. DeHoog and L. S. Eberlin, *Anal. Chem.*, 2019, **91**, 4266–4290.
2 J. A. Fincher, A. R. Korte, B. Reschke, N. J. Morris, M. J. Powell and A. Vertes, *Analyst*, 2017, **142**, 3157–3164.
3 P. Nemes and A. Vertes, *Anal. Chem.*, 2007, **79**, 8098–8106.
4 Z. Takats, J. M. Wiseman, B. Gologan and R. G. Cooks, *Science*, 2004, **306**, 471–473.
5 R. B. Cody, J. A. Laramee and H. D. Durst, *Anal. Chem.*, 2005, **77**, 2297–2302.
6 O. Golf, N. Strittmatter, T. Karancsi, S. D. Pringle, A. V. M. Speller, A. Mroz, J. M. Kinrosss, N. Abbassi-Ghadi, E. A. Jones and Z. Takats, *Anal. Chem.*, 2015, **87**, 2527–2534.
7 J. M. He, F. Tang, Z. G. Luo, Y. Chen, J. Xu, R. P. Zhang, X. H. Wang and Z. Abliz, *Rapid Commun. Mass Spectrom.*, 2011, **25**, 843–850.
8 R. B. Dixon, M. S. Bereman, D. C. Muddiman and A. M. Hawkridge, *J. Am. Soc. Mass Spectrom.*, 2007, **18**, 1844–1847.
9 J. Balog, T. Szaniszlo, K. C. Schaefer, J. Denes, A. Lopata, L. Godorhazy, D. Szalay, L. Balogh, L. Sasi-Szabo, M. Toth and Z. Takats, *Anal. Chem.*, 2010, **82**, 7343–7350.
10 J. Balog, L. Sasi-Szabo, J. Kinross, M. R. Lewis, L. J. Muirhead, K. Veselkov, R. Mirnezami, B. Dezso, L. Damjanovich, A. Darzi, J. K. Nicholson and Z. Takats, *Sci. Transl. Med.*, 2013, **5**, 194ra93.
11 D. L. Phelps, J. Balog, L. F. Gildea, Z. Bodai, A. Savage, M. A. El-Bahrawy, A. V. M. Speller, F. Rosini, H. Kudo, J. S. McKenzie, R. Brown, Z. Takats and S. Ghaem-Maghami, *Br. J. Cancer*, 2018, **118**, 1349–1358.
12 R. B. Dixon, J. S. Sampson, A. M. Hawkridge and D. C. Muddiman, *Anal. Chem.*, 2008, **80**, 5266–5271.
13 J. S. Sampson, K. K. Murray and D. C. Muddiman, *J. Am. Soc. Mass Spectrom.*, 2009, **20**, 667–673.
14 S. H. Jeong, O. V. Borisov, J. H. Yoo, X. L. Mao and R. E. Russo, *Anal. Chem.*, 1999, **71**, 5123–5130.
15 B. Hattendorf, C. Latkoczy and D. Gunther, *Anal. Chem.*, 2003, **75**, 341A–347A.
16 S. N. Jackson, J. K. Kim, J. L. Laboy and K. K. Murray, *Rapid Commun. Mass Spectrom.*, 2006, **20**, 1299–1304.

17 Z. Y. Chen, A. Bogaerts and A. Vertes, *Appl. Phys. Lett.*, 2006, **89**, 041503.

18 Z. Y. Chen and A. Vertes, *Phys. Rev. E: Stat., Nonlinear, Soft Matter Phys.*, 2008, **77**, 036316.

19 D. Bleiner and A. Bogaerts, *Spectrochim. Acta, Part B*, 2007, **62**, 155–168.

20 S. J. M. Van Malderen, A. J. Managh, B. L. Sharp and F. Vanhaecke, *J. Anal. At. Spectrom.*, 2016, **31**, 423–439.

21 L. R. Compton, B. Reschke, J. Friend, M. Powell and A. Vertes, *Rapid Commun. Mass Spectrom.*, 2015, **29**, 67–73.

22 M. Guillong, H. R. Kuhn and D. Gunther, *Spectrochim. Acta, Part B*, 2003, **58**, 211–220.

23 D. Bleiner and D. Gunther, *J. Anal. At. Spectrom.*, 2001, **16**, 449–456.

24 A. M. Leach and G. M. Hieftje, *Appl. Spectrosc.*, 2002, **56**, 62–69.

25 W. Su, L. Zhu, P. Wang, Y. Zhang and L. Wu, *J. Comput. Phys.*, 2020, **407**, 109245.

26 F. Cao, F. Donnarumma and K. K. Murray, *Analyst*, 2016, **141**, 183–190.

27 I. Apitz and A. Vogel, *Appl. Phys. A*, 2005, **81**, 329–338.

28 C. Y. Liu, X. L. Mao, J. Gonzalez and R. E. Russo, *J. Anal. At. Spectrom.*, 2005, **20**, 200–203.

29 P. Nemes, H. H. Huang and A. Vertes, *Phys. Chem. Chem. Phys.*, 2012, **14**, 2501–2507.

30 H. Lindner, D. Autrique, J. Pisonero, D. Gunther and A. Bogaerts, *J. Anal. At. Spectrom.*, 2010, **25**, 295–304.

31 K. L. Bischoff, Glucosinolates, in *Nutraceuticals*, ed. R. C. Gupta, Elsevier, London, 1st edn, 2016, pp. 551–554.

32 R. Shroff, K. Schramm, V. Jeschke, P. Nemes, A. Vertes, J. Gershenzon and A. Svatos, *Plant J.*, 2015, **81**, 961–972.

33 U. Wittstock, D. J. Kliebenstein, V. Lambrix, M. Reichelt and J. Gershenzon, in *Integrative Phytochemistry: From Ethnobotany to Molecular Ecology*, ed. J. Romeo, Elsevier, Amsterdam, 2003, vol. 37, pp. 101–125.

Electronic Supplementary Information

Remote Ablation Chamber for High Efficiency Particle Transfer in Laser Ablation Electrospray Ionization Mass Spectrometry

Marjan Dolatmoradi,‡[a] Jarod A. Fincher,‡[a] Andrew R. Korte,[a] Nicholas J. Morris,[b]
and Akos Vertes*,[a]

[a] *Department of Chemistry, The George Washington University, Washington, DC 20052, USA*
[b] *UES, Inc., Beavercreek, OH 45432, USA*

**Corresponding author*
E-mail: vertes@gwu.edu, Phone: +1 (202) 994-2717, Fax: +1 (202) 994-5873.

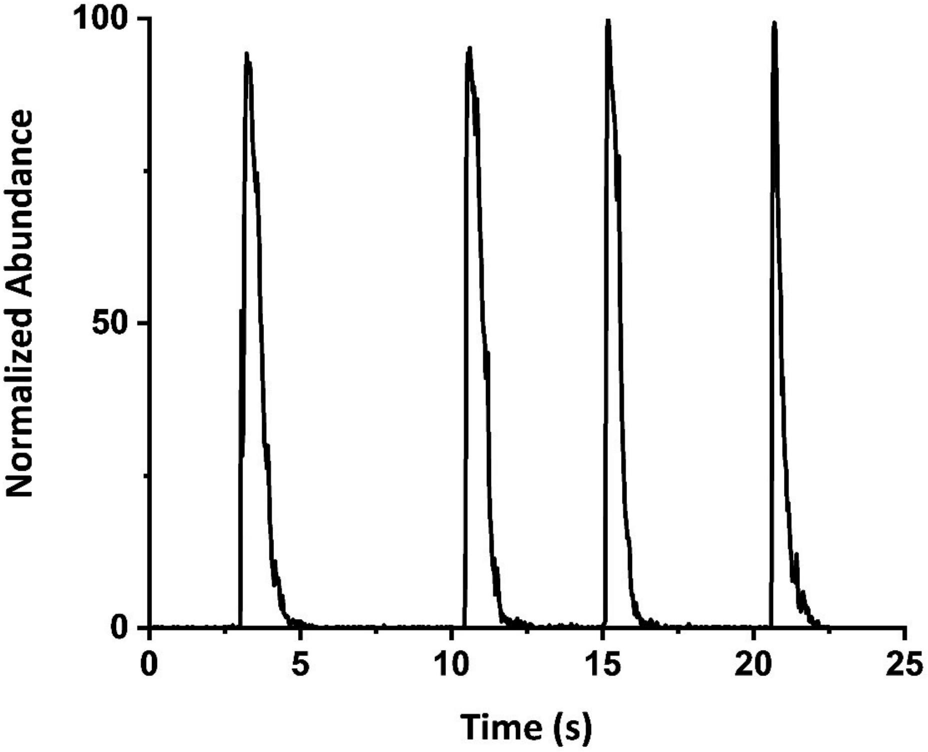

Figure S1: Temporal profile of verapamil signal for four single laser pulses impinging on tissue phantom in modified ablation chamber. No sample carryover is observed.

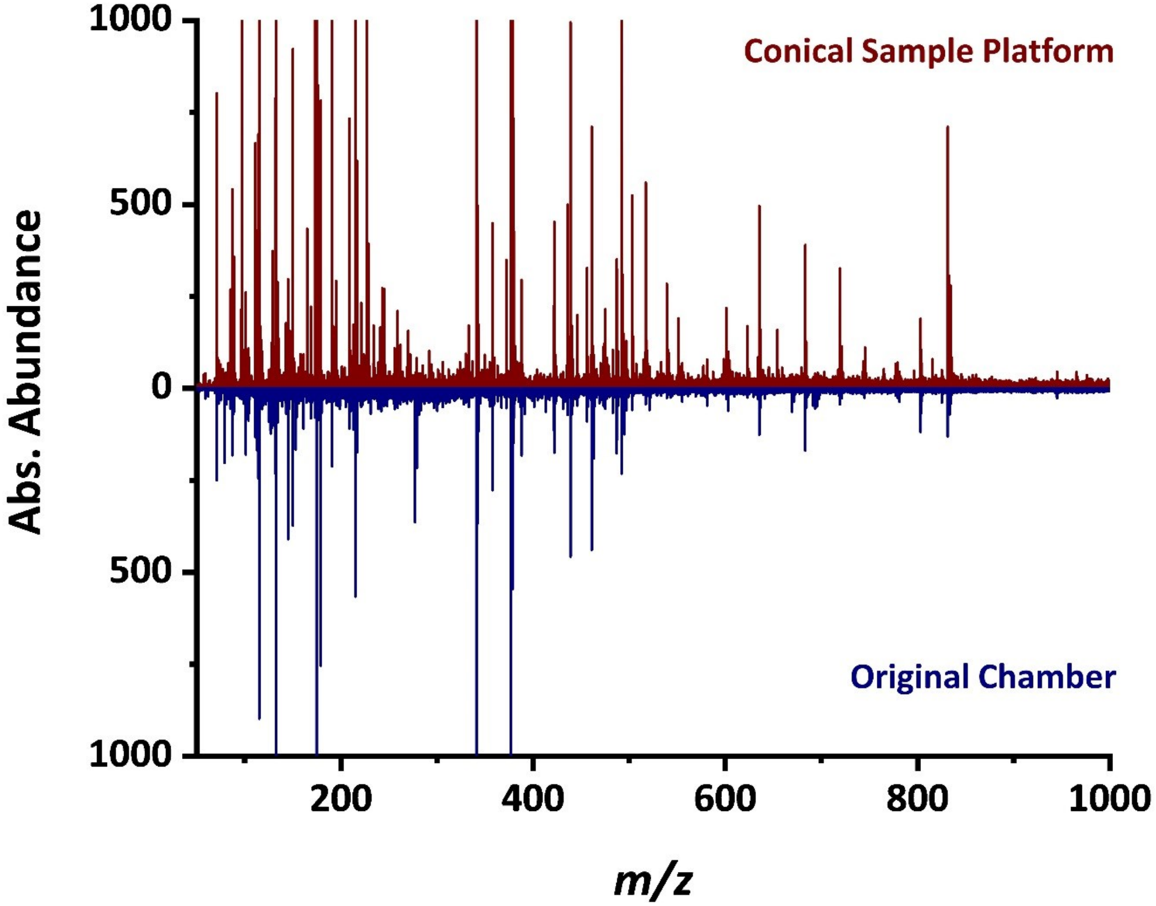

Figure S2: Zoomed-in views of mass spectra obtained from Brussels sprout (*B. oleracea*) stem sections using original and modified ablation chambers. After background subtraction, 129 and 106 peaks were detected for the modified and original chambers, respectively.

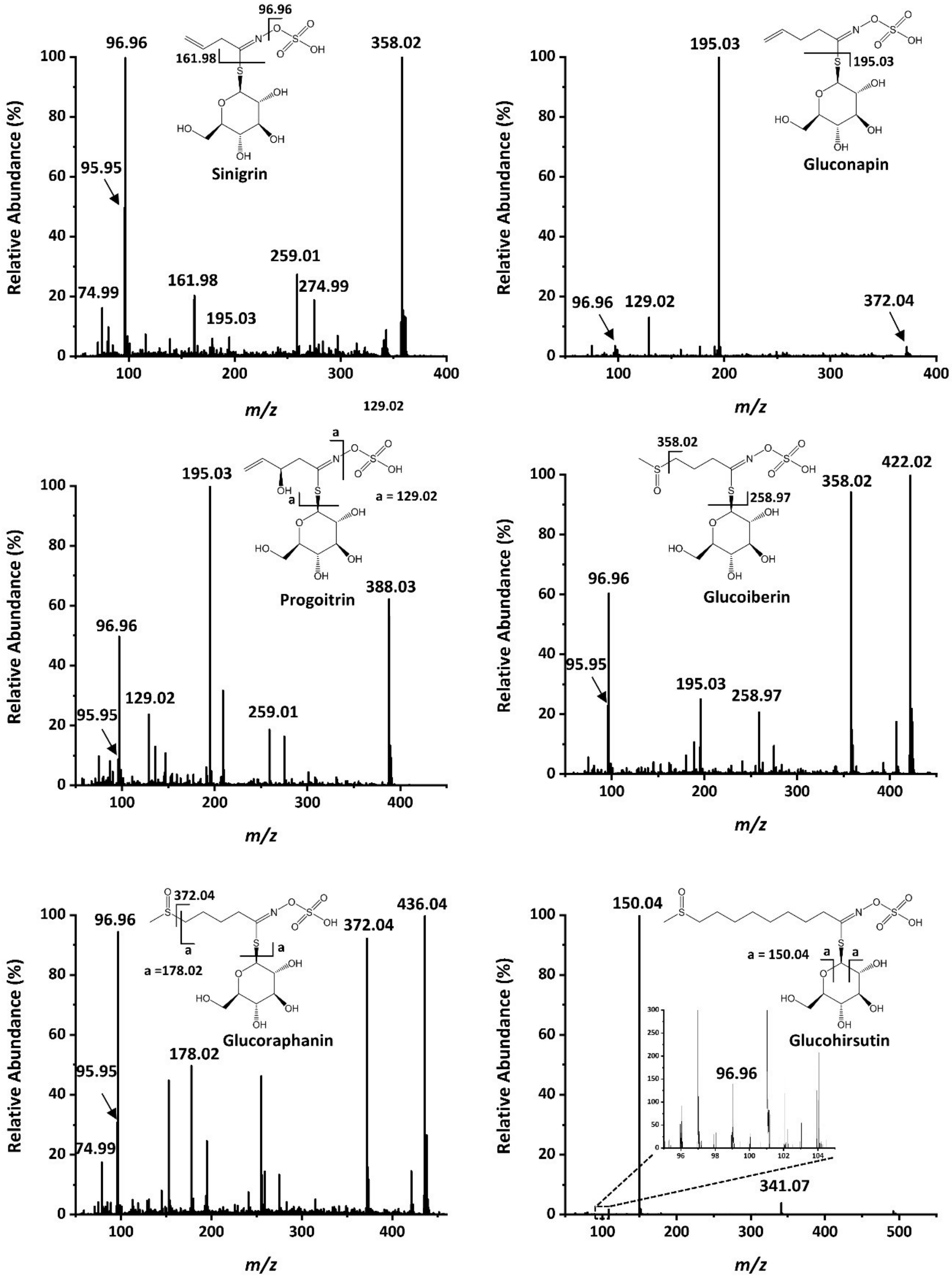

Figure S3: Tandem mass spectra for six glucosinolates from Brussels sprout (*B. oleracea*) stem sections.